Journal of Power Sources 695 (2026) 241374

Contents lists available at ScienceDirect

Journal of Power Sources

journal homepage: www.elsevier.com/locate/jpowsour

Ultra-low loading and ionomer-free anodes for cost-effective PEM water electrolysis using successive ion layer adsorption and reaction (SILAR)

S. Delgado [a], E. Sousa [a], V. Pereira [a], C. Fernandes [a], K.A. Friedrich [b], A. Mendes [a,*]

[a] LEPABE – Laboratory for Process Engineering, Environment, Biotechnology and Energy, ALiCE – Associate Laboratory in Chemical Engineering, Faculty of Engineering, University of Porto, Rua Dr. Roberto Frias, Porto, 4200-465, Portugal
[b] Institute of Engineering Thermodynamics/Electrochemical Energy Technology, German Aerospace Center (DLR), Pfaffenwaldring 38-40, Stuttgart, 70569, Germany

HIGHLIGHTS

- Novel ionomer-free Ir electrodes fabricated on Ti felts via SILAR method.
- Fluorination of TiO_2 strongly enhanced IrO_x OER activity through favourable electronic effects.
- Fluorination boosted OER activity 400-fold within the fluorinated series.
- Ultra-low Ir loading (<0.4 mg cm^{-2}) shows superior stability *vs.* IrO_2 PTL.

ARTICLE INFO

Keywords:
Proton exchange membrane water electrolyzers
Ultra-low Ir loading
SILAR
Cost-effective
PFAS-Free

ABSTRACT

While iridium catalysts offer a good balance of activity and stability for the oxygen evolution reaction (OER) in acidic media, their high cost, coupled with the limitations of perfluorosulfonic acid (PFSA) membranes and ionomers, hinders large-scale Proton Exchange Membrane (PEM) water electrolysis. This work addresses these challenges by introducing a novel ionomer-free electrode design. Porous titanium felts were engineered with a thin iridium oxide layer using sequential ion layer adsorption and reaction (SILAR). Crucially, surface fluorination via NH_4F treatment significantly enhanced OER performance, leading to a drastic decrease in onset potential and a 400-fold higher OER current density for the optimal F6.8 composition compared with the least active composition within fluorinated series. The prepared ultra-low iridium loading porous transport electrodes (<0.4 mg cm^{-2}) maintained excellent activity while demonstrating superior stability than the IrO_2 porous transport layer reference under intensive potential cycling tests. This approach paves the way for cost-effective and durable PEM water electrolyzers by minimizing noble metal usage and ruling out the expensive and toxic PFSA-based ionomer.

1. Introduction

Novel energy storage solutions are crucial to harnessing the full potential of renewable energy sources. Water electrolysis emerges as a critical technology in this transition. By 2050, the green hydrogen market is projected to reach a staggering 27 000 TWh/year of energy consumption, equivalent to a production of 500 Mt/year of hydrogen, representing 18 % of global energy consumption [1]; this requires electrolyzers ranging from gigawatt (GW) to terawatt (TW) scale. Nevertheless, there is currently no technology for producing green hydrogen in large quantities via water electrolysis. The proton exchange membrane water electrolyzers, one of the most promising technologies, is still prohibitively expensive due to the use of high loadings of precious group metals (PGMs) as catalysts, Iridium and Platinum, and bulk titanium-based porous transport layers (PTLs) and bipolar plates (BPPs) to withstand the harsh acidic environment and anodic potentials. These factors combined account for about 75 % of the cost of the electrolyzers, making it less competitive compared to grey hydrogen produced primarily from methane steam reforming [2]. Naturally, as the active area and number of cells per stack increase, the amount of raw materials needed for making both bipolar plates and anode PTLs will grow proportionally. This translates to higher upfront costs (capital costs) [3]. Simultaneously, to compete with alternative energy sources, achieving a target cost of $\leq$ 2 €/kg H_2 [4] requires significant reductions in the

* Corresponding author.
E-mail address: mendes@fe.up.pt (A. Mendes).

https://doi.org/10.1016/j.jpowsour.2026.241374
Received 27 July 2026; Received in revised form 12 August 2026; Accepted 26 August 2026
Available online 28 August 2026
0378-7753/© 2026 The Authors. Published by Elsevier B.V. This is an open access article under the CC BY license (http://creativecommons.org/licenses/by/4.0/).

overall cost of electrolyzers, improved system efficiencies, longer component lifetimes, and the development of alternative materials to replace scarce PGMs [5].

In reality, the natural supply of Ir, one of the rarest elements on the planet, with an annual mining output of approximately 7 ton/year, will be the biggest bottleneck in the following years [6]; even if half of the world's yearly Ir supply was allocated entirely to fabricate Proton Exchange Membrane (PEM) electrolyzers, only a few GW-scale electrolyzers could be deployed if typical Ir loadings continue to be applied (*i.e.*, 1-3 mg $_{Ir}$ cm^{-2}). Consequently, developing low-loaded yet highly efficient anodes (0.1-0.5 mg_{Ir} cm^{-2}) is paramount to successfully implementing such systems. Actually, it has been shown that nanostructured thin films display great mass activity for oxygen evolution reaction (OER) while employing ultra-low loadings (0.25 mg_{Ir} cm^{-2}) [7].

Moreover, a critical bottleneck hindering performance improvements in PEM water electrolyzers is the active passivation of titanium-based anode PTLs. This phenomenon makes it extremely difficult to identify alternative materials that can surpass the performance of titanium itself [8]; nonetheless, numerous solutions have arisen to lower contact resistance and/or improve performance during lengthy periods of operation [9]. One of them is the sputtering of low iridium loadings on Ti-PTL-Based felts (<0.1 mg_{Ir} cm^{-2}), which has been assigned to increase electrical conductivity and hence reduce the interfacial contact resistance (ICR) to 60 mΩ cm^2 [10]. Coatings with other precious metals, such as Au or Pt, are another option, albeit the latter require thicker and denser layers, and produce less conductive oxides [11]. For instance, some unexplored yet potential attempts to enhance the electrical conductivity may involve the fluorination of the porous transport layers. In standard approaches for other electrochemical systems, such as lithium-ion batteries or photocatalysis, fluorine-doped titanium dioxide (F-TiO_2) particles or films are often used as photoanodes to enhance light absorption efficiency and electrical conductivity [12]. For these cases, fluorine doping is commonly accomplished via chemical vapor deposition (CVD) or atomic layer deposition (ALD). However, CVD typically requires very precise control over temperature, pressure, and chemical reactions, while ALD generally has slower deposition rates compared to other methods.

However, thin film deposition of active catalysts at room temperature and ambient pressure is also possible using successive ion layer adsorption and reaction (SILAR) technology [13,14]. This process relies on a layer-by-layer approach and, unlike other techniques, operates in a solution phase, enabling versatile control over film properties. Also, the SILAR method allows for precise control of particle size, the surface features of the electrocatalysts and the thickness of the films, which is achieved by fine-tuning the duration of each step: adsorption, reaction, and rinsing [15]. These features are essential since they are required to reduce the Ir loading in PEMWE anodes without compromising their stability [16]. In this context, direct electrodeposition of Ir onto Ti-based substrates represents an attractive route for preparing electrocatalysts with low Ir loadings, offering short deposition times and potential compatibility with continuous processing [17]. However, when applied to highly porous, three-dimensional Ti felts, deposition is governed by spatial variations in electrode potential, current density, electrolyte accessibility and mass transport. These factors may result in non-uniform Ir nucleation and growth across the external and internal surfaces of the felt. This limitation is particularly relevant when ultra-low catalyst loadings are targeted on anodized Ti felts, because the surface TiO_2 layer introduces additional electrical and interfacial resistance that may restrict electron transfer at the deposition sites. The successive ionic layer adsorption and reaction (SILAR) approach provides an alternative that relies on repeated adsorption, chemical reduction, and rinsing steps, thereby largely decoupling Ir deposition from the externally imposed current distribution. Although SILAR generally requires longer processing times, catalyst loading can be conveniently adjusted by varying the number of deposition cycles. Electrodeposition and SILAR may therefore be regarded as complementary, whose relative suitability depends on the substrate architecture, target catalyst loading, required deposition uniformity and process-scale-up requirements. Similarly, nanostructured thin-film (NSTF) electrodes represent an important benchmark for low-Ir-loading PEM water electrolysis, owing to their highly optimized catalyst architecture and excellent reported mass activity [18]. In contrast, the SILAR electrodes developed in this work were fabricated entirely by solution-phase processing at ambient temperature and pressure. This approach enables direct deposition of the Ir catalyst onto the final three-dimensional Ti-felt porous transport layer, without requiring vacuum processing or incorporation of an ionomer into the catalyst layer. Although NSTF electrodes benefit from a well-established fabrication platform and highly optimized catalyst utilization, SILAR provides a simpler solution-based route that is directly applicable to porous three-dimensional substrates and does not require vacuum-deposition infrastructure. Nevertheless, further process optimization and scale-up studies are required to establish whether SILAR can achieve the uniformity, reproducibility and production throughput required for large-scale manufacturing.

Aside from guaranteeing homogeneous dispersion of catalytic materials, fine-tuning the morphology/pore structure of PTL should be ensured to improve catalyst utilization and provide smooth support for ultra-thin membranes. Several methods have been developed to enhance the surface area of PTLs in PEMWE. These include chemical etching, anodization, and template-based methods [19].The latter involves incorporating polymers or silica into the PTL during fabrication and removing them, leaving behind a PTL replica of the template's pore characteristics. This approach allows for the precise tuning of the PTLs with specific pore structures, which can improve their performance. However, the scalability of this method remains a significant challenge. On the other hand, anodization is also a promising method. This electrochemical process is used for modifying and increasing the natural oxide layer on metal surfaces; the metal to be treated serves as the anode (positive electrode) in an electrolyte bath. When an electric current is applied, it triggers controlled oxidation, resulting in the formation of an engineered surface with interesting optical and microstructural features for catalysis [4].

Membranes and ionomers represent a minor cost fraction (5 %) [4] of the PEMWE stack, but they contribute considerably to polarization losses [20], reducing the overall performance of PEMWE significantly.

As the preferred solid polymer electrolyte (SPE) for PEMWEs, for membrane and ionomer, Nafion is a member of the per- and polyfluoroalkyl substances (PFAS) class, which is recognized for its exceptional environmental persistence [21,22]. On the other hand, the production and degradation of the perfluorinated polymers (PFOs) involve the release of PFAS, which accumulates in groundwater, raising concerns about potential health risks [23]. Therefore, the European Chemicals Agency (ECHA) proposed a restriction on the production and use of PFAS in February 2023 [24]. This process has progressed substantially since then: an updated proposal published in August 2025, extending the assessment to eight additional sectors [25], and the scientific evaluation expected to conclude by the end of 2026. Motivated by the substantial economic and health impacts of PFAS contamination, this proposal seeks to develop strategies for minimizing their environmental release. But this fight will be difficult because of the huge difference between the production cost (~19 €/kg) and the estimated cost of healthcare and environmental cleanup (>18 k€/kg) [26]. Notably, PFAS exhibit high environmental persistence and require specialized high-temperature incineration (>1400 °C) [27]. In this regard, the PEMWE market should be significantly impacted by the EU's ban on PFASs, as PEMWE systems may become even more expensive.

This work proposes an innovative approach for producing catalyst-integrated gas diffusion electrodes dismissing the use of ionomers made of Nafion [28] and ruling out the need for high loadings of Iridium. The used SILAR technique facilitates the deposition of ultra-thin,

ultra-low-loading iridium nanoparticle films (<0.4 mg_{Ir} cm^{-2}), paving the way for a potential revolution in water electrolysis. In addition, this research explores the intricate interplay between three key factors: fluorine doping, number of SILAR cycles, and anodization conditions. By optimizing these parameters, it was possible to develop electrodes characterized by peak efficiency and remarkable stability for PEMWE applications.

2. Experimental section

2.1. Preparation of titanium felts

Anodic TiO_2 layers were prepared by anodizing Ti felts from Bekaert. The Ti felts were degreased by sonication in acetone, ethanol, and deionized (DI) water for 20 min, then dried in an N_2 stream. Anodization was carried out in a typical three-electrode cell employing an Ag/AgCl saturated 3 M KCl electrode as the reference electrode, a graphite rod as the counter electrode, and the titanium felt as the working electrode. The electrolyte solution included 3 M HCl. The anodization procedure was carried out by continually bubbling the electrolyte with N_2 and applying 1 V or 5 V for 10 s. The Ti felts were thoroughly rinsed, submerged in DI water for 2 h after anodization and then dried overnight at 100 °C.

2.2. Deposition of metallic nanoparticles on TiO_2-etched surface

SILAR was used to deposit iridium nanoparticles on anodized Ti felts. The TiO_2 substrates were progressively exposed to an Ir salt precursor, $IrCl_3{\cdot}xH_2O$ (Sigma Aldrich), and sodium borohydride ($NaBH_4$) solutions to deposit Ir nanocrystallites. Ti substrates were submerged in 0.5 mg/mL $IrCl_3{\cdot}xH_2O$ solution for 60 s, then in $NaBH_4$ solution (1 mg/mL) for another 60 s before being rinsed with DI water for 20 s. This SILAR procedure was repeated 120, 360, and 740 cycles to allow for the growth of the catalytic nanoparticles over the substrate.

2.3. Addition of fluorine to titanium felts

Before the deposition of metallic Ir nanoparticles via SILAR, some samples were immersed in NH_4F solutions for 2 h after adjusting the pH of the solution to 2 with HCl. Several aqueous concentrations of NH_4F were studied, namely 1.7, 3.4, 6.8, 13.6 and 27.2 mmol. After that, the samples were thoroughly rinsed with DI water and annealed at 500 °C for 5 h at a heating rate of 3 °C min^{-1} to produce F-TiO_2 structures over the Ti felts. Ir nanoparticles were afterwards deposited via SILAR.

2.4. Materials characterization

The Scanning Electron Microscopy and Energy-Dispersive X-ray Spectroscopy (SEM/EDS) examination was conducted using a High Resolution (Schottky) Environmental Scanning Electron Microscope with X-ray microanalysis and Electron Backscattered Diffraction (EBSD) analysis: FEI Quanta 400 FEG ESEM/EDAX Genesis X4M for morphological characterization. Cross-sectional image samples were prepared by manually cracking the surface using liquid nitrogen. The resulting specimens were then placed onto carbon tape adhered to a supporting pin for subsequent analysis. Magnifications ranging from 600× to 2500x were employed. X-ray photoelectron spectroscopy (XPS, Kratos Axis Ultra HAS at CEMUP, Porto) was utilized to characterize the composition and chemical state of the films. The spectra were shifted about the C 1s signal at 284.8 eV, and peaks were fitted using CasaXPS software.

2.5. Measurement of electrochemical properties

A three-electrode cell configuration was used to pre-screen the OER activity of prepared Ir-doped Ti felts PTLs. 1 cm^2 active area Ti felt was used as working electrode, a graphite rod served as counter electrode and an Ag/AgCl worked as reference electrode. The electrolyte was kept at room temperature and was composed of 0.1 M $HClO_4$.

Initially, 3 pre-conditioning potential cycles were performed in the OER window (1.3 V to 2.5 V_{RHE}) at 100 mV s^{-1}. Electrochemical Impedance Spectroscopy (EIS) was conducted in potentiostatic mode, employing a 10 mV perturbation at a high-frequency range (999 mHz – 1 kHz) to evaluate the ohmic drop. The ohmic resistance obtained from the high-frequency x-intercept of the EIS spectra was used to apply 100 % *i R*-compensation, using a single fixed resistance value per sample, to all polarization curves reported in this work, including the commercial IrO_2 benchmark, ensuring a consistent basis for comparison across all samples. The OER activity was measured during linear sweep voltammetry (LSV) (1.3 V – 2.5 V *vs*. Reversible Hydrogen Electrode (RHE) at 20 mV s^{-1}) in an Ar-saturated electrolyte. During the measurements, a gas blanketing system was implemented to prevent electrolyte contamination from the cell's exterior. A cyclic voltammogram (CV) was recorded from 0.05 V to 1.4 V using a scan rate of 20 mV s^{-1}. Subsequently, an LSV was recorded from 1.3 V to 2.5 V *vs*. RHE to quantify the OER mass activity of each catalyst.

The electrochemical active surface area (ECSA) was assessed based on the electrochemical double-layer capacitance (C_{dl}), obtained via cyclic voltammograms (CV) conducted at various scan rates within the non-faradaic region spanning from 0.9 V to 1.5 V_{RHE}. This approach was employed owing to the well-established relationship between ECSA and C_{dl} for a given material, as expressed by the equation $C_{dl} = i_c/v$. Here, C_{dl} represents the double-layer capacitance in Farads per square centimeter (mF cm^{-2}). In contrast, i_c and v denote the charging current in milliamperes per square centimeter (mA cm^{-2}) and the scan rate in millivolts per second (mV s^{-1}). Additionally, the copper under-potential deposition (Cu UPD) method was used to validate the ECSA findings. Initially, the electrode was immersed in a purged (Ar) 0.1 M H_2SO_4 electrolyte at 0.05 V *vs*. RHE for 10 min to reduce the reversible iridium oxide species formed during catalyst synthesis. The electrode was then cycled within the potential range from 0.2 V to 0.72 V *vs*. RHE at 20 mV s^{-1} to acquire a background CV. Subsequently, the electrode was again reduced for 15 min at 0.05 V. The original electrolyte was then replaced by a 0.5 M H_2SO_4 electrolyte containing 5 mM of Cu_2SO_4 (Merck). The electrolyte was purged with Ar for half an hour to remove the dissolved oxygen. Finally, the electrode was cycled for 5 times (0.2 V to 0.72 V *vs*. RHE at 20 mV s^{-1}) to obtain the Cu UPD voltammogram. Copper has a similar ionic radius to metallic iridium, 128 p.m. and 136 p.m., respectively. By initially maintaining the electrode at 0.05 V and cycling it under these potentials, each Cu atom will adsorb and desorb on the surface of each iridium atom. Integrating the UPD (stripping) peak area makes it possible to determine the abundance of active Ir sites from each catalyst.

The performance and stability of the prepared Ti-felt PTLs were then evaluated in a PEM water electrolyzer single cell. Two graphite bipolar plates, hydrophilic carbon paper (Sigracarb 2050, Fuel Cell Store) at the cathode side, and each prepared Ir-doped Ti porous transport layer at the anode, were compressed onto a Nafion 115 membrane, which was positioned at the center to construct a PEM water electrolyzer (6.25 cm^2). Four screws were tightened to a torque of 2 N m to hold the cell.

Each PEM electrolyzer containing the prepared PTL was characterized by performing polarization curves at 60 °C using a slew rate of 10 mV s^{-1} and retrieving electrochemical impedance spectra in potentiostatic mode (1.8 V). An accelerated stress test (AST) was conducted to evaluate the best-performing system's stability by applying 3000 cycles within the OER window at 60 °C. The performance of the cell was re-evaluated after the AST.

3. Results and discussion

This study proposes the direct engineering of a nanostructured IrO_x thin film onto a titanium (Ti) felt substrate for producing a highly active

electrode for the OER. This eliminates the need for separate catalyst synthesis and ink preparation encompassing toxic ionomers; the preparation process becomes then simplified.

The disclosed process involved three steps, as illustrated in Fig. 1, including: i) growth of a Ti support**:** anodization of the Ti felt in an acidic environment to generate a nanostructured support, enhancing the surface area and creating anchoring sites for the catalyst; ii) iridium deposition: successive ion layer adsorption and reaction (SILAR) [29], while using iridium chloride ($IrCl_3$) as metal precursor and sodium borohydride ($NaBH_4$) as reducing agent, allowing the depositing of a thin, uniform Ir film with controlled thickness; iii) fluorine doping: an additional doping step with ammonium fluoride (NH_4F) solution was implemented to enhance the conductivity and stabilize the iridium nanoparticles during electrolysis.

3.1. Anodization of pure Ti felts

Scanning electron microscope images (Fig. 2 (a) and 2 (b)) reveal the remarkable transformation of the titanium felt surface after anodization. Fig. 2 (a) shows the pristine surface, while Fig. 2 (b) depicts the felt after being treated with an acidic electrolyte (3 M HCl) at 1 V for 15 s. Notably, the anodization process successfully creates a customized surface texture on the titanium fibers. This texture is rougher and more porous compared to the initial smooth surface. The anodization promotes the hydrolysis of the titanium felt, producing a thicker layer of TiO_2, which is very stable in aqueous and acidic conditions – low free energy of formation of TiO_2 (-820 kJ mol^{-1}) [30,31]. Thereupon, Ir was dispersed via successive layer adsorption and reaction (SILAR) method to generate a thin Ir layer of nanoparticles.

A three-electrode cell setup - Figure S1 (a) and (b) **-** was used to assess the OER activity of the prepared electrodes at room-temperature, 0.1 M $HClO_4$ (aq) solution, as depicted in Fig. 2 (c). The electrode that underwent anodization shows a remarkable ability to perform the OER compared to the untreated sample (pristine), and the titanium felt that only went through SILAR cycles without prior anodization; the OER onset occurs at a lower potential, *ca.* 1.82 V_{RHE} compared to the non-anodized sample *ca.* 1.87 V_{RHE}, at a current density of $j = 1$ mA cm^{-2}. The anodized sample achieved a two-fold larger limiting current density, indicating improved mass transport. These findings may be a direct result of the anodization of the Ti substrate – the porous oxide layer that is formed, TiO_2, greatly increases the surface area; a larger surface area typically is translated into more active sites, which in turn leads to the observed higher current densities [32,33]. Moreover, the porous structure facilitates the diffusivity of reactants and products to and from the reaction sites, improving the overall reaction efficiency [34].

The anodization process results in a thicker double-layer capacitance due to increased surface roughness, as evidenced by the cyclic voltammetry (CV) curves recorded at 20 mV s^{-1} for the various electrodes, as shown in Fig. 2 (d). This is because electrodes with a larger surface area can typically accumulate more ions at the interface, leading to a larger double-layer capacitance (C_{dl}) [33].

It is possible to further fine-tune the properties of the anodized oxide Ti layer and yield a larger active surface area to boost OER by optimizing the anodization parameters, which include the electrolyte concentration and/or composition, the input potential on the working electrode and duration of the anodization step, as well as the temperature [34,35]; Fig. S2 explores the direct impact of boosting the anodization potential to 5 V on both surface area and OER charge transfer resistance (R_{ct}). The results indicate a dependence of double layer capacitance (C_{dl}) and R_{ct} on the applied potential; the sample anodized at 5 V exhibits a 15 % reduction in R_{ct} compared to its 1 V anodized counterpart. This significant improvement strongly suggests that the exposure of additional active iridium sites is facilitated by the surface area.

3.2. Optimization of SILAR deposition method

A modified SILAR method was used to produce thin-film anodes; the anodized TiO_2 felt was first immersed in the cationic solution of $IrCl_3$ for 60 s (0.5 mg mL^{-1}), then in the anionic solution of $NaBH_4$ (mg mL^{-1}) also for 60 s, and finally the substrate was rinsed in distilled water for 30 s [36,37]. This sequence cycle was then repeated for 120, 360 and 740 times.

Fig. 3 (a) shows the polarization curves of the prepared anodes and reveals a trend of progressively decreasing OER onset potential with the number of cycles. The electrode with 740 cycles displays an iridium loading of 0.40 ± 0.06 mg cm^{-2} and reached 1 mA cm^{-2} at 1.55 V_{RHE}. For comparison, the electrode cycled 360 times displays an iridium loading of 0.20 ± 0.04 mg cm^{-2} and onset at 1.9 V_{RHE}, and the electrode cycled 120 times displays an iridium loading of 0.06 ± 0.02 mg cm^{-2} onset at 2.0 V_{RHE}, for the same current density, *cf.* Fig. 3b).

Fig. 3(c–f) presents SEM images of the TiO_2 felts decorated with iridium prepared using 120, 360, and 740 SILAR cycles, respectively. These images show Ir round-shaped nanoparticles over the titanium surface, increasing in concentration with the number SILAR cycles. Additionally, Fig. S4 suggests a slight decrease in the average particle size as the number of SILAR cycles increase. The Ir particles dispersed on sample "740″ exhibit a Gaussian size distribution with an average diameter of 16.03 nm and a standard deviation of 0.32 nm. In contrast, the sample prepared with 360 SILAR cycles presents a larger average particle size and size dispersion of 19.09 ± 1.26 nm – *cf.*, supplementary

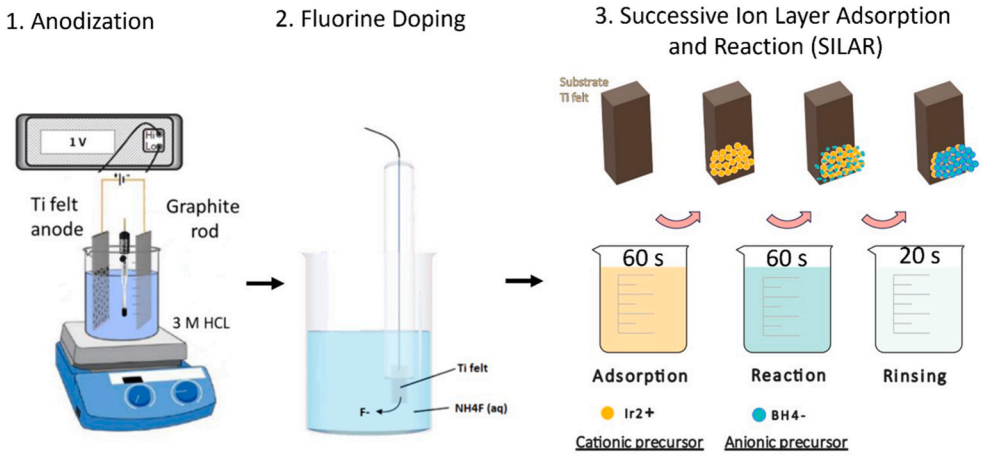


Fig. 1. Schematics of the preparation steps of Titanium decorated felt with IrO_x nanostructures using anodization, fluorine immersion bath doping and successive ion layer adsorption and reaction (SILAR).

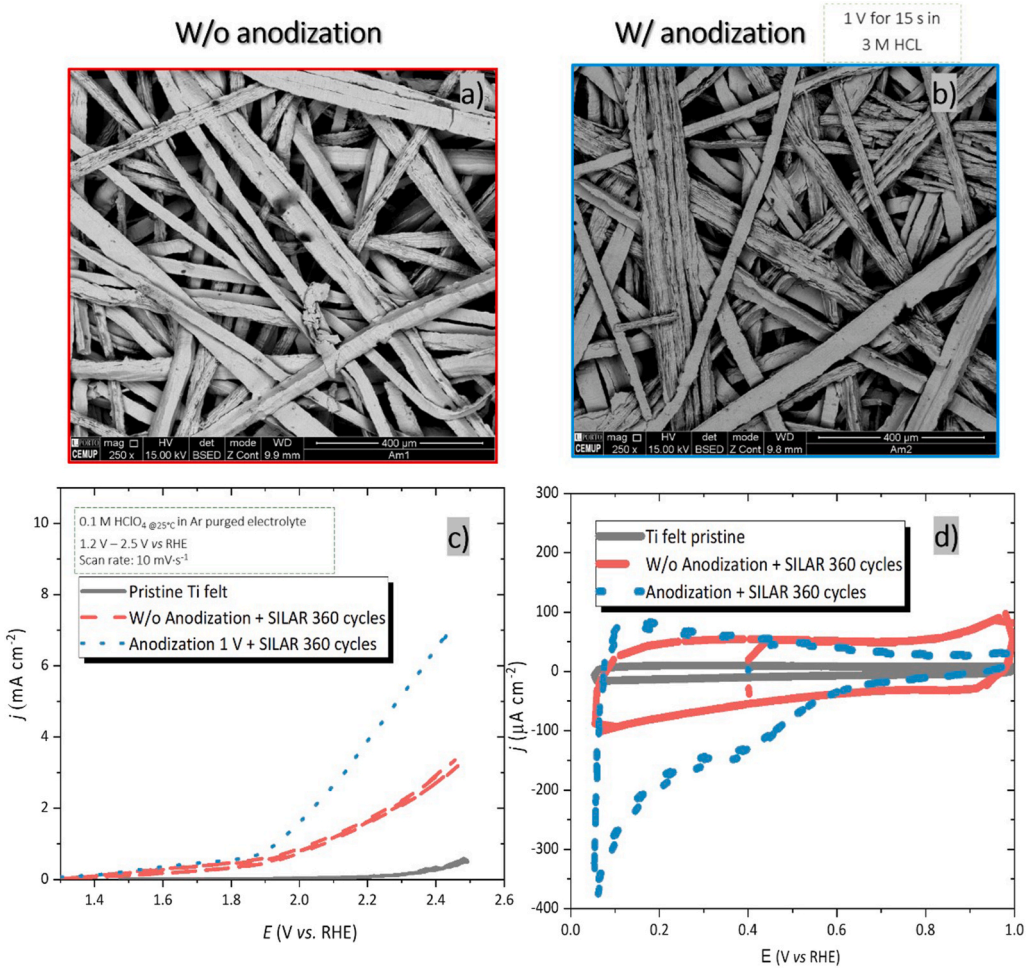


Fig. 2. SEM images of **(a)** pristine Ti felt without (W/o) anodization and **(b)** as-anodized (W/) Ti Felt at 250x magnification; **(c)** OER LSV and **(d)** CV curves of the Ir decorated anodized/pristine Ti felts, at 1 V and room temperature in a 3 M HCL aqueous solution.

information Figure S4 (b) and (d).

Overall, the SILAR technique allowed for the fabrication of binder/ionomer-free electrodes with ultra-low iridium loadings (<0.4 mg cm^{-2}) and Ir nanoparticles ranging from 16 to 19 nm of average diameter [3,38]. This method stands out for its simplicity, efficiency, and exceptional reproducibility, which are critical advantages over traditional approaches, namely roll-to-roll like screen-printing and slot die.

3.3. *Fluorine doping effect on performance*

A sequence of experiments was conducted to evaluate the influence of fluorine doping on the TiO_2 surface and especially the outcome in terms of electrical conductivity. Following anodization at 1 V, TiO_2 felts were immersed in NH_4F solutions with fluorine concentrations of 1.7, 3.4, 6.8, 13.6, and 27.2 mmol for a period of 3 h. These samples were named F-*x*, where *x* represents the fluorine concentration. Iridium was then deposited using the SILAR technique, where 360 cycles were applied to reach the ultra-low loading of 0.2 mg_{Ir} cm^{-2}.

The surface composition of the prepared substrates was investigated using XPS. The XPS spectra (Fig. S5) reveal the presence of Ir, Ti, and O; however, F is not readily identifiable; a dedicated scan of the F 1s region (Fig. S6) did not yield a discernible photoelectron peak above the background noise for any fluorinated samples, precluding reliable identification and quantification of F by XPS under acquisition conditions, likely reflecting the combined effect of the low F content and the count-limited statistics typical of narrow-window scans for trace elements [39].

Fig. S7 depicts a compelling trend: all IrO_x catalysts supported on F-doped TiO_2 exhibit a negative shift in their Ir 4f orbital binding energies compared to IrO_x supported onto non-doped Ti felts with or without anodization, *i.e.,* IrO_x/TiO_2 or IrO_x/Ti, respectively. This observation strongly suggests an electron transfer process from F-doped TiO_2 to the active IrO_x catalyst [40]. Furthermore, increasing F-doping of the TiO_2 substrate, a progressively lower binding energy is observed for the Ir $4f^7/_2$ peak. This can be attributed to a higher electron density surrounding the Ir atoms as the F-doping concentration increases; consequently, the electrostatic attraction between the core electrons and the nucleus weakens, making them easier to remove during XPS [41]. Quantitatively, the Ir $4f^7/_2$ binding energy of sample F6.8 ($[F^-]$ = 6.8 mmol) is 61.90 eV, a 1.0 eV and 1.10 eV lower compared to the sample F1.7 ($[F^-]$ = 1.7 mmol) and bare IrO_x supported on titanium samples, respectively (cf., *supplementary information* Figure S7 and Table S1).The deconvolution of the Ir 4f XPS spectra (Fig. S8) revealed the presence of Ir^0 (4f [7]/$_2$/$4f^5/_2$ orbitals), Ir^{4+} (4f [7]/$_2$/$4f^5/_2$ orbitals) and Ir^{3+} species; the corresponding quantitative analysis is presented in Table S1 and Table S2. No metallic Ir^0 species were detected in the IrO_x/F-TiO_2 (F6.8) sample, which had the greatest Ir^{4+} concentration (90.54 %). The remaining concentration was attributed to Ir^{3+} species, which is normally found in more amorphous Ir structures. Recent mechanistic studies on Ir-based OER catalysts revealed the formation of reactive electrophilic oxygen species, O^{1-}, within mixed-valent Ir^{3+}/Ir^{4+} hydrated amorphous oxyhydroxides (IrO_x) [42,43]. These findings suggest that these species play a crucial role in enhancing the

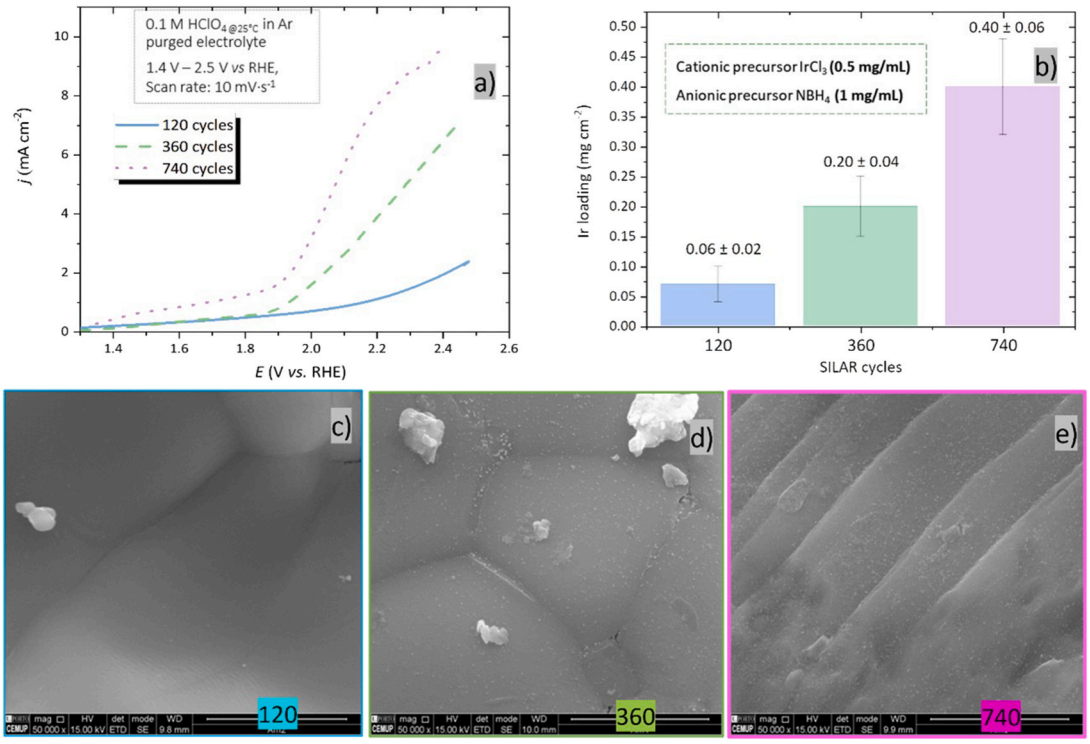


Fig. 3. **(a)** OER performance of Ti felt electrodes decorated with Ir nanoparticles corresponding to 120, 360 or 740 SILAR cycles in a three-electrode setup; **(b)** number of SILAR cycles and Ir average mass loading; **(c,d,e)** Top-view SEM images of Ir decorated felts prepared with 120, 360 or 740 SILAR cycles at 50 000x.

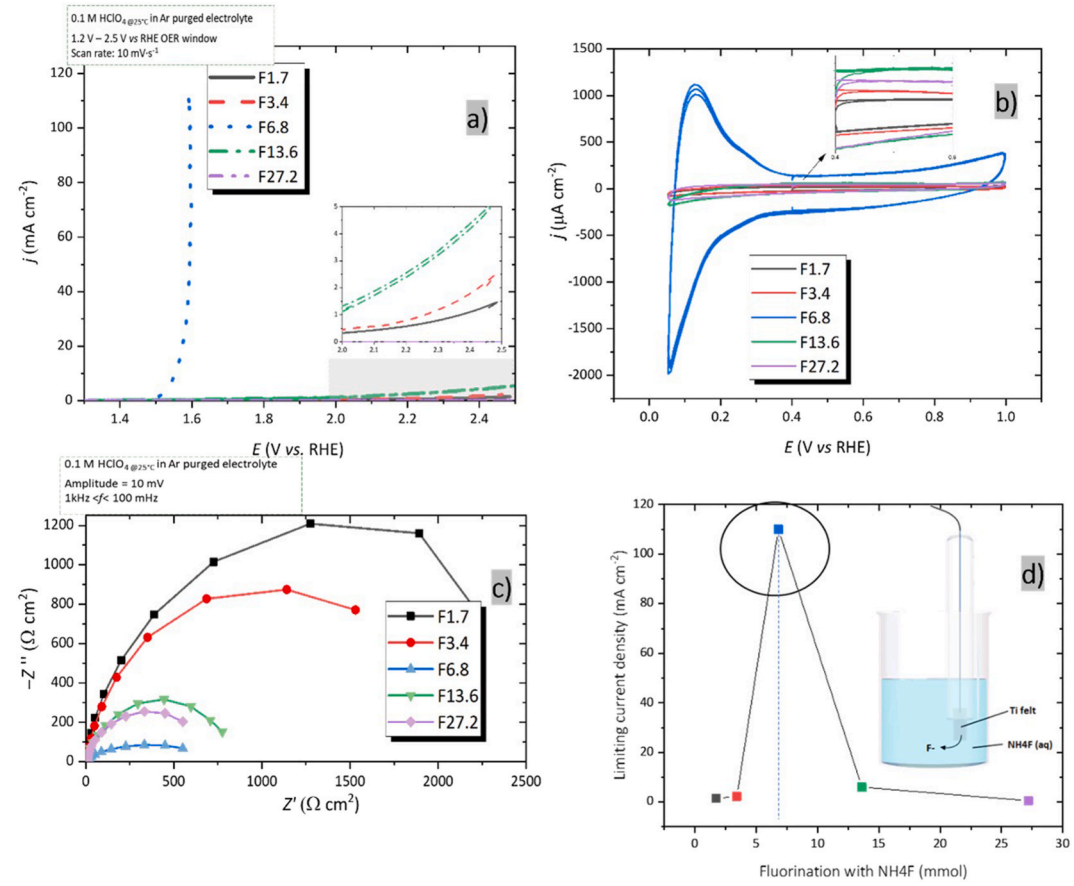


Fig. 4. **(a)** OER activity for Ir decorated F-TiO_2 substrates prepared by varying the degree of fluorination (1.7, 3.4, 6.8, 13.6 and 27.2 mmol) **(b)** CV spectra of the Ir decorated F-TiO_2 substrates **(c)** EIS spectra measured at 1.6 V_{RHE} and **(d)** Fluorination degree as a function of limiting current density.

activity of amorphous IrO_x compared to their more crystalline counterparts, which is the case of the remaining prepared samples (F1.7, F3.4, IrO_x/Ti and IrO_x/TiO_2).

Fig. 4 (a) depicts the OER performance of the synthesized Ir-decorated F-TiO_2 samples, measured in a three-electrode cell configuration. The data indicates an apparent threshold effect concerning the fluorine doping concentration. Specifically, increasing F-doping concentrations up to 6.8 mmol seems to impact positively the OER; beyond this threshold, the presence of fluorine has a detrimental effect. The F6.8 sample, which was prepared following a mass ratio of $NH_4F:TiO_2$ of *ca.* 6 % (corresponding to 6.8 mmol), exhibits the highest OER activity and limiting current density among all the investigated F-doped catalysts; in this particular case and at $j = 1$ mA cm^{-2} the OER onset occurs at 1.52 V_{RHE}, and the limiting current density is 118 mA cm^{-2}. The enhancement in OER limiting current density may be partly due to an increase in surface-active area. This is supported by Fig. 4 (b), which shows a direct correlation between F-doping concentration and the charge double layer which is proportional to the electrochemically active surface area (ECSA) – up to the optimal value F6.8. At high current densities, however, the limiting current is also governed by mass-transport phenomena within the porous electrode. Recent studies have shown that hierarchical or multichannel pore architectures can enhance reactant/product transport and facilitate gas-bubble removal, while surface wettability and pore-size distribution strongly influence bubble detachment and mass-transfer resistance [43,44]. These effects are particularly relevant for PTL architectures, where efficient water access and rapid removal of evolved O_2 can help preserve the accessibility of catalytic sites at high current densities. Thus, the enhanced limiting current observed for the F6.8 electrode may arise not only from its higher electrochemically accessible surface area, but also from favourable mass-transport characteristics of the porous electrode architecture. Additionally, Fig. S9 confirms a greater concentration of Ir near the surface of sample F6.8 compared to F3.4, for instance. The EDS, which assesses the composition up to a depth of 3 μm, indicates a higher concentration of catalyst on the F6.8 sample.

Notably, the F6.8 electrode – identified as the optimum composition within the fluorinated series, Fig. 4 (d) - exhibited an approximately 400-fold higher OER current density than the least active composition within the prepared electrodes under identical SILAR conditions and differing only in degree of fluorination - Fig. 4 (a). This self-benchmark comparison illustrates the fluorination degree on the OER performance of the SILAR-deposited IrO_x catalyst, with F6.8 representing the optimal balance between beneficial and detrimental effects of F-doping.

EIS, performed at a potential difference of 1.6 V_{RHE}, was employed to further assess the effect of F-doping concentration on Ti felts, as shown in Fig. 4 (c). The radii corresponding to the low-frequency semicircles in the plots, which are indicative of charge transfer resistance, R_{ct}, follow a distinct trend: IrO_x/F-TiO_2 (F6.8) displays the smallest radius and then the lowest R_{ct} value (512 Ω cm^2) compared to F27.2 (720 Ω cm^2), F13.6 (723 Ω cm^2), F3.4 (2250 Ω cm^2) or F1.7 (2500 Ω cm^2). This sequence highlights the enhanced charge-transfer kinetics achieved by the F6.8 sample during the OER, consistent with its improved catalytic performance. The R_{ct} represents the resistance associated with interfacial charge transfer in the OER at the IrO_x/electrolyte interface. The lower R_{ct} achieved for F6.8, together with the increase in R_{ct} at higher F contents, indicates that the beneficial effect of fluorination on interfacial charge transfer is not monotonic. This behaviour is consistent with the progressive shift in Ir $4f_{7/2}$ binding energy discussed above and may reflect a balance between the favourable electronic modification of the TiO_2 support at moderate fluorination levels and detrimental changes arising at higher F contents.

3.4. Evaluation of surface-active area and conductivity of F-doped Ti felts

The ECSA of the most OER active sample – F6.8, was assessed using the copper underpotential deposition (CuUPD) charge method and compared to a benchmark IrO_2 catalyst deposited onto a pretreated (anodized) TiO_2 felt (Fig. 5 (a) *vs.* Figure S10 (a)). The samples went through an electrochemical reduction stage before characterization, to ensure complete copper ion sorption. This involved applying a potential of 0.5 V_{RHE} for 10 min. The prepared F6.8 sample boasts a 1.63-fold increase in active iridium sites for the OER compared to the commercial IrO_2 sample, as seen in Fig. 5 (b). This substantial increase aligns perfectly with the observed enhancement in OER activity per unit mass (mass activity) for sample F6.8, cf. Fig. S11 in supplementary information.

Moreover, the capacitive charge (C_{dl}) of sample F6.8 was estimated based on cyclic voltammograms and used to compare with the Premetek sample. As the Ir loading of these two samples is similar, the capacitive charge should be directly proportional to the active surface area. Following, the normalized interfacial charge obtained from the CVs (Figure S9 (b) and (c)) shows that sample F6.8 owns an approximately 1.6-fold higher active surface area (*ca.* 8×10^{-3} mF cm^{-2}) compared to the Premetek sample (*ca.* 4×10^{-3} mF cm^{-2}) [39], which corroborates the results obtained based on the Cu_{UPD} measurements. The pronounced increase in active surface area aligns also with the well-dispersed IrO_x nanoparticles shown in SEM micrographs (Fig. 5(c) and (d)). Together with the lower R_{ct} observed for F6.8, these results indicate that the enhanced OER performance is associated with both more favourable interfacial charge-transfer kinetics and increased accessibility and utilization of Ir active sites.

The IrO_x nanoparticles applied via SILAR on F-doped TiO_2 felts compared to undoped Ti felts (cf.,- Fig. 3 (d)) clearly indicate that F-doped Ti felt allows the growth of more homogeneous and small catalyst particle size. This enhanced dispersion was assigned to the formation of reduced Ti^{3+} species during the F-doping process, especially at fluorine concentrations of 6.8 mmol; the Ti^{3+} sites, have an increased electron density and positive charge deficiency, acting as solid adsorption sites for negatively charged $IrCl_6^{2-}$ precursor ions during the SILAR synthesis procedure; besides, other factors such as surface defects or modifications in surface acidity due to F-doping could also contribute to the ensuing more uniform Ir nanoparticles distribution.

The four-point probe method was used to measure the electrical conductivity of the prepared samples for two compression values, 100 cN m and 200 cN m, as shown in Fig. 5 (e). The measurements revealed a significant increase in electrical conductivity for IrO_x/F-TiO_2 (F6.8) compared to the undoped felts and the felt prepared by spraying commercial IrO_2 catalyst particles. At 100 cN m, sample F6.8 exhibits the highest conductivity of 0.28 S cm^{-1}. This value is higher than the obtained for the undoped TiO_2 felts (0.26 S cm^{-1}) or commercial IrO_2 sprayed over a Ti felt (0.125 S cm^{-1}). The fluorinated TiO_2 display Ti^{3+} centers that enhance the electrical conductivity of the Ti felt, as an extra electron is localized in the t_2g orbital of Ti, just below the conduction band minimum, as seen in Table S1 [45].

3.5. PEMWE performance and the influence of ionomer

The developed ionomer-free fluorine doped anode PTL, prepared by SILAR, *i.e.,* IrO_x/F-TiO_2 (F6.8), was compared with a conventional electrode in a single cell PEMWE. The conventional electrode, named "Commercial IrO_2 + Nafion," was prepared following the guidelines for the production of catalyst layers using an ionomer-to-catalyst ratio (I/C) of 0.3; the two anodes were prepared to display the same iridium loadings and two loadings were considered, 0.2 mg_{Ir} cm^{-2} and 0.4 mg_{Ir} cm^{-2}.

In a PEM water electrolyzer, the Nafion ionomer typically act as a binder to hold the catalyst particles together and facilitate proton conduction to and from the membrane and within the electrode; therefore, the total proton conductivity in hydrated Nafion is secured by three contributors: (i) bulk water conductivity via Grotthuss diffusion (or structural diffusion) mechanism - this is the main mechanism - where protons hop between hydrogen-bonded water molecules without the

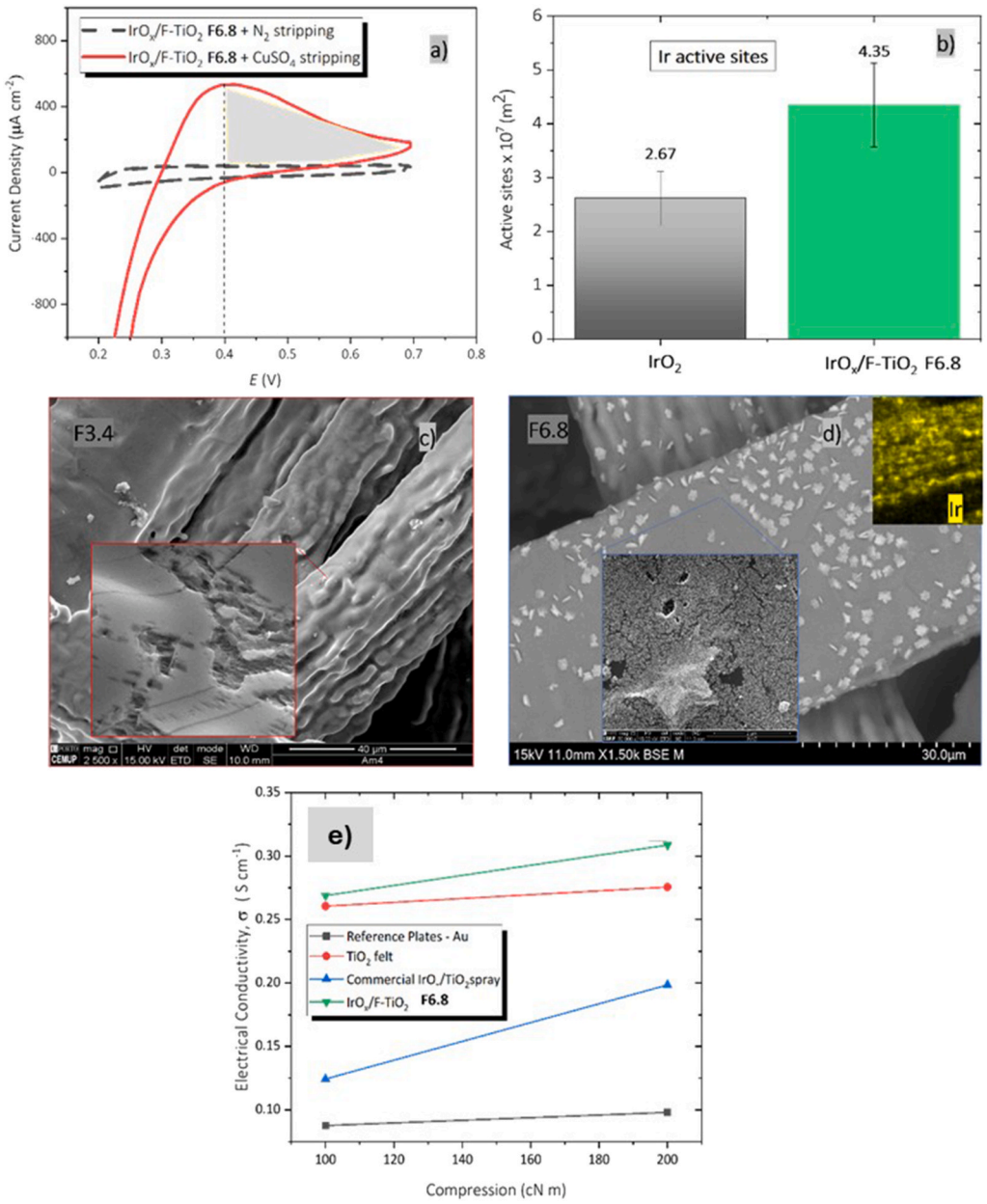


Fig. 5. **(a)** CV demonstrating Cu_{UPD} method applied to F6.8 sample**; (b)** Number of active sites for catalysts layers composed of commercial IrO_2 from Premetek and SILAR prepared IrO_x/F-TiO_2; SEM top-view images of **(c)** IrO_x/F-TiO_2 (F2) and **(d)** F6.8 samples at 2500 X; **(e)** Electrical conductivity at two compression stages, 100 cN m and 200 cN m.

need for the entire molecule to move, (ii) bulk water conductivity via vehicular diffusion where protons are transported as part of hydronium ions (H_3O^+), though this process is generally slower than the Grotthuss mechanism because it involves the diffusion of larger [46], solvated ions [47]; and (iii) by surface polymer conductivity via proton hopping from one sulfonate group present in Nafion to the next [48]. However, the conventional sprayed electrodes loaded with an ionomer seem to consistently underperform compared to their ionomer-free counterparts, regardless of whether fluorinated Ti-felt or plane Ti-felt is used as support, despite the ultra-low iridium loadings used, 0.2 mg_{Ir} cm^{-2} or 0.4 mg_{Ir} cm^{-2} - Fig. 6 (a). The conventional electrodes exhibited higher electrical resistance (ohmic overpotential) and underwent more significant mass-transport limitations than the ionomer-free IrO_x electrodes. In detail, the prepared ionomer-less IrO_x/F-TiO_2 electrodes achieve 2-fold higher limiting current densities compared to the benchmark electrode at 2.5 V and 80 °C. This is likely due to a combination of factors, as when catalyst ink is directly applied by spraying, it can seep into the pores of the PTL, trapping catalyst particles and reducing their accessibility for the oxygen evolution reaction [49].This inefficient catalyst utilization can be further amplified at lower catalyst loadings. The EIS spectra recorded at 1.6 V in Fig. 6 (b) show the ionomer-free F6.8 PTL owns superior catalytic activity, evident from the much smaller charge transfer resistances <1 Ω cm^2, corroborating with its lower activation overpotential, *i.e.*, *ca.* 225 mV, Fig. 6 (a).

The F6.8 PTL demonstrates significantly higher initial activity compared to the Benchmark PTL, showing approximately 30 times greater performance as evidenced by the Tafel slope analysis. This enhanced activity indicates that the ionomer-free F6.8 electrode, prepared using the SILAR technique, likely exposes a greater number of Ir active sites for reaction compared to the benchmark PTL, thereby optimizing Ir utilization [49,50]. This argument is further supported by two key observations: first, the IrO_x/F-TiO_2 sample exhibits nearly twice the

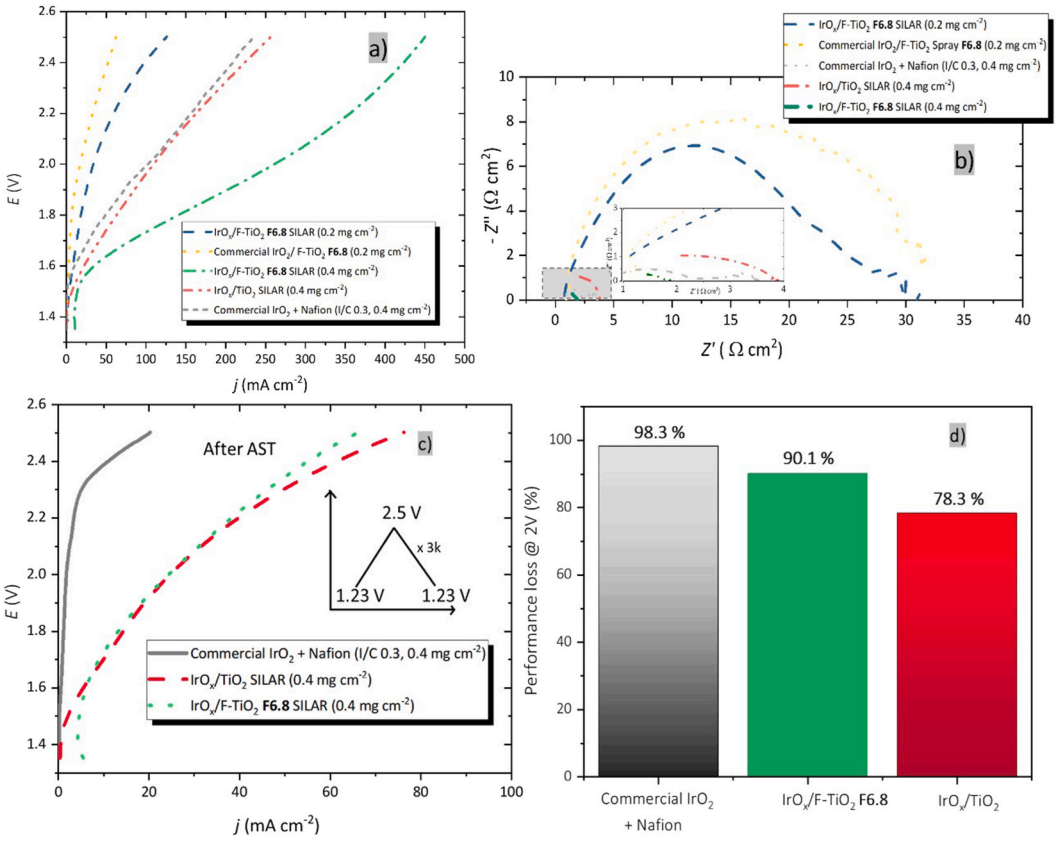


Fig. 6. Polarization curves **(a)** and **(b)** EIS spectra recorded at 1.6 V for ionomer-free F3 PTLs and ionomer-coated commercial IrO_2 based PTLs; **(c)** end-of-life (EoL) performance of 0.4 mg_{Ir} cm^{-2} PTLs after accelerated stress test and **(d)** performance loss at 2 V. Measurements recorded at 80 °C and PTLs with Ir loadings of 0.2 and 0.4 mg cm^{-2}.

number of active sites compared to the commercial catalyst, as shown in Fig. 5 (b); then, the OER mass activity at 1.55 V_{RHE} is approximately double for F6.8 (60 A g^{-1}) compared to the IrO_2 felt (36 A g^{-1}), as illustrated in Fig. S11.

The enhanced interfacial charge-transfer kinetics of F6.8 identified in half-cell measurements are also reflected in the single-cell PEMWE performance. As shown in Fig. 6 (b), the F6.8 electrode exhibits a markedly lower charge-transfer resistance (R_{ct}) and high-frequency ohmic resistance than both the undoped IrO_x/TiO_2 electrode and the commercial IrO_2/Nafion benchmark. The high-frequency resistance comprises the ohmic contributions of the electrolyte or membrane, the F-TiO_2/Ti-felt substrate and interlayer, and the electrical contacts. Together with the higher electrochemically active surface area and improved IrO_x nanoparticle dispersion discussed above, these results indicate that F6.8 provides a favourable balance between the beneficial electronic, interfacial and morphological effects of fluorination and the detrimental effects that emerge at higher fluorine contents.

While the prepared ultra-low iridium loading PTLs demonstrate promising activity, exceeding that of benchmarks based on mixed-phases (amorphous and crystalline), IrO_2, they still fail to achieve the desired 2 A cm^{-2} target at 2 V [51]. This highlights the need for further optimization. A key challenge lies in balancing reduced Ir molar fraction with performance. As Yuang et al. recently pointed out [52], decreasing Ir loading diminishes the interface area between the catalyst and transport layers.

However, the proposed approach of utilizing a conductive fluorinated interlayer presents a promising solution. This interlayer acts as an effective bridge between the substrate and the catalyst particles, facilitating rapid charge transfer processes and ensuring excellent electrical conductivity. Moreover, the electrochemical data suggests that the continuous water access to the catalyst surface may provide pathway for proton conduction at the electrode, both to and from the membrane, through Grotthuss and vehicular mechanisms. This is particularly evident in the absence of an ionomer network at the electrode.

The PEMWE equipped with the ultra-low loading F-doped IrO_x/F-TiO_2 (F6.8) PTL, prepared without ionomer, underwent long-term stability testing following modified EU-harmonized protocols (3000 cycles, 1.23-2.5 V, 80 °C). The end-of-life performance was then compared with that of undoped (IrO_x/TiO_2) and commercially available IrO_2/Nafion electrodes, as shown in Fig. 6 (c).

The F6.8 PTL exhibited a markedly improved stability compared to the commercial counterpart. Notably, the F6.8 PTL maintained a low onset overpotential of only 442 mV at the end-of-life (EoL) and at 5 mA cm^{-2}, representing a near 60 % reduction compared to the commercial IrO_2 + Nafion PTL (1123 mV). These findings demonstrate markedly lower degradation of the F6.8 PTL than that of commercial IrO_2/Nafion electrode. This behaviour may be associated with the direct integration of the IrO_x nanoparticles onto the nanostructured TiO_2 support through the SILAR, which may favour strong catalyst-support interactions and limit catalyst redistribution or agglomeration during operation.

The observed trend in stability persists even at higher current densities (2 V), when mass transport limitations become more significant. Following the AST protocol, the commercial catalyst exhibited a near-complete loss of functionality, even using Nafion ionomer as a binder for the catalytic particles, with a 98.3 % decrease in current density. In contrast, the ionomer-less F6.8 PTL displayed a demonstrably lower degradation loss of approximately 90 %, Fig. 6 (d). Guoqiang Li et al. [39] investigated the electrocatalytic performance of Ir/F-TiO_2 electrodes prepared by the sol-gel method, demonstrating exceptional electrocatalytic activity and stability. The catalyst layer exhibited also remarkable stability with minimal Ir leaching. It preserved structural

integrity after 10 h under a constant 1.55 V potential, surpassing the performance of IrO_2 even at a catalyst loading of 1 mg cm^{-2}.

Notably, the prepared F6.8 PTL experienced a slightly higher degradation rate than the undoped counterpart. This observation indicates that fluorination does not necessarily improve durability and highlights a trade-off between the enhanced initial activity provided by F doping and long-term stability. The higher degradation of the F6.8 electrode may be associated with changes in the fluorinated surface during prolonged operation, including possible fluorine loss [53], although this mechanism was not directly quantified in the present work. Nevertheless, the substantially higher initial activity of F6.8 results in a higher retained absolute performance throughout the AST compared with the undoped electrode, while the F6.8 PTL remains considerably more stable than the commercial IrO_2/Nafion benchmark.

Beyond the stability considerations discussed above, the observed performance of the ionomer-free electrode can be rationalized by considering the three-phase reaction environment within the porous PTL. In conventional catalyst layers, the ionomer provides proton-conducting pathways between catalyst particles and the membrane. In the present architecture, however, the IrO_x nanoparticles are directly deposited onto the conductive F-TiO_2/Ti felt network, providing a continuous electronic pathway to the current collector, while the open porous structure allows continuous access of liquid water to the catalyst surface and removal of the generated O_2. Thus, the IrO_x/electrolyte interface may itself provides the reaction environment where water access proton transport and electronic conduction can be simultaneously established without an ionomer binder. The higher limiting current density and lower charge-transfer resistance observed for the ionomer-free F6.8 electrode - Fig. 6(a) and (b) - support the effectiveness of this architecture for reactant/product transport and interfacial charge transfer. Nevertheless, the absence of an ionomer may limit proton-conducting pathways between the catalyst and the membrane, particularly for IrO_x deposited within PTL pores or in regions lacking intimate membrane contact. Consequently, some catalyst sites may experience local proton-transport limitations or remain electrochemically inaccessible. Despite this potential limitation, the results indicate that, at the ultra-low Ir loadings and under the operating conditions investigated, direct catalyst integration into the PTL provides adequate electronic connectivity and sufficiently short proton-transport pathways to sustain OER activity without requiring a continuous ionomer phase within the catalyst layer.

4. Conclusions

This work demonstrates a novel surface engineering approach for preparing ionomer-free IrO_x/F-TiO_2 (F6.8) OER catalysts on titanium felts. Combining anodization, SILAR with iridium precursors, and surface fluorination resulted in a 400-fold higher OER current density for the optimal F6.8 composition relative to the least active composition within the same fluorinated series, highlighting the substantial, non-monotonic role of F-doping degree in the activity of SILAR-deposited IrOx. Notably, F-doping (6.8 mmol) of the TiO_2 substrate enhanced the electronic interaction with the IrO_x catalyst nanoparticles, leading to denser and size homogeneous layers of catalyst particles. This translated into exceptional electrocatalytic activity, with the F6.8 catalyst exhibiting a remarkably low onset overpotential of solely 241 mV at 5 mA cm^{-2}. Furthermore, the novel ionomer-free OER electrode displayed superior performance and long-term stability than state-of-the-art anodes, suggesting a potentially revolutionary pathway for PEM water electrolysis using promising low iridium loadings – 0.2 mg cm^{-2}. In fact, the conventional sprayed electrodes using Nafion ionomers consistently underperform compared to the ionomer-free counterparts, regardless of fluorine doping. This was evidenced at ultra-low iridium loadings of 0.2 mg_{Ir} cm^{-2} and 0.4 mg_{Ir} cm^{-2}, where the advantage of using an ionomer becomes less significant. Furthermore, the obtained electrochemical evidences suggest that for the production of ultra-thin layers, supplying water to the PEMWE anode is sufficient to ensure full proton conduction through the electrode via both the Grotthuss and vehicular mechanisms. This may eliminate the need for complex ionomer networks at these low iridium loadings. This work paves the way for a more sustainable, rapid, cost-effective manufacturing process for critical components, promoting non-toxic fabrication methods.

CRediT authorship contribution statement

S. Delgado: Writing – original draft, Methodology, Investigation, Data curation, Conceptualization. **E. Sousa:** Writing – review & editing, Investigation. **V. Pereira:** Methodology, Investigation. **C. Fernandes:** Writing – review & editing. **K.A. Friedrich:** Writing – review & editing, Supervision. **A. Mendes:** Writing – review & editing, Supervision, Resources, Project administration.

Declaration of competing interests

The authors declare that they have no known competing financial interests or personal relationships that could have appeared to influence the work reported in this paper.

Acknowledgements

This work was supported by national funds through FCT/MECI: LEPABE, UID/00511/2025 (https://doi.org/10.54499/UID/00511/2025) and UID/PRR/00511/2025 (https://doi.org/10.54499/UID/PRR/00511/2025) and ALiCE, LA/P/0045/2020 (https://doi.org/10.54499/LA/P/0045/2020). Also, by project Baterias 2030, with the reference POCI-01-0247-FEDER-046109, co-funded by Operational Programme for Competitiveness and Internationalisation (COMPETE 2020), under the Portugal 2020 Partnership Agreement, through the European Regional Development Fund (ERDF). S.Delgado, E.Sousa,. V. Pereira and C.Fernandes are pleased to thank the Portuguese Foundation for Science and Technology (FCT) for the doctoral grants with reference SFRH/BD/144338/2019, SFRH/BD/145412/2019, SFRH/BD/143218/2019 and 2021.07014.BD, respectively.

Appendix A. Supplementary data

Supplementary data to this article can be found online at https://doi.org/10.1016/j.jpowsour.2026.241374.

Data availability

Data will be made available on request.

References

[1] Global Hydrogen Review 2021 – Analysis - IEA. https://www.iea.org/reports/global-hydrogen-review-2021 (accessed 2024-April-25).
[2] M. Chatenet, B.G. Pollet, D.R. Dekel, F. Dionigi, J. Deseure, P. Millet, R.D. Braatz, M.Z. Bazant, M. Eikerling, I. Staffell, P. Balcombe, Y. Shao-Horn, H. Schäfer, Water electrolysis: from textbook knowledge to the latest scientific strategies and industrial developments, Chem. Soc. Rev. 51 (11) (2022) 4583–4762, https://doi.org/10.1039/D0CS01079K.
[3] J.K. Lee, G. Anderson, A.W. Tricker, F. Babbe, A. Madan, D.A. Cullen, J.D. Arregui-Mena, N. Danilovic, R. Mukundan, A.Z. Weber, X. Peng, Ionomer-free and recyclable porous-transport electrode for high-performing proton-exchange-membrane water electrolysis, Nat. Commun. 14 (1) (2023) 1–11, https://doi.org/10.1038/s41467-023-40375-x, 2023 14:1.
[4] L. Bertuccioli, A. Chan, D. Hart, F. Lehner, B. Madden, E. Standen, Study on Development of Water Electrolysis in the EU, 2014. Lausanne, Switzerland.
[5] P. Shirvanian, F. van Berkel, Novel components in proton exchange membrane water electrolyzers (PEMWE): Status, challenges and future needs, Electrochem. Commun. (2020) 106704, https://doi.org/10.1016/j.elecom.2020.106704. Elsevier Inc. May 1.
[6] C. Minke, M. Suermann, B. Bensmann, R. Hanke-Rauschenbach, Is iridium demand a potential bottleneck in the realization of large-scale PEM water electrolysis? Int. J. Hydrogen Energy 46 (46) (2021) 23581–23590, https://doi.org/10.1016/J.IJHYDENE.2021.04.174.

[7] T. Hrbek, P. Kúš, Y. Kosto, M.G. Rodríguez, I. Matolínová, Magnetron-sputtered thin-film catalyst with low-ir-ru content for water electrolysis: long-term stability and degradation analysis, J. Power Sources 556 (2023) 232375, https://doi.org/10.1016/J.JPOWSOUR.2022.232375.

[8] C. Rakousky, U. Reimer, K. Wippermann, M. Carmo, W. Lueke, D. Stolten, An analysis of degradation phenomena in polymer electrolyte membrane water electrolysis, J. Power Sources 326 (2016) 120–128, https://doi.org/10.1016/J.JPOWSOUR.2016.06.082.

[9] A.S. Gago, S.A. Ansar, B. Saruhan, U. Schulz, P. Lettenmeier, N.A. Cañas, P. Gazdzicki, T. Morawietz, R. Hiesgen, J. Arnold, K.A. Friedrich, Protective coatings on stainless steel bipolar plates for proton exchange membrane (PEM) electrolysers, J. Power Sources 307 (2016) 815–825, https://doi.org/10.1016/j.jpowsour.2015.12.071.

[10] C. Liu, M. Shviro, S.F. Zaccarine, A.S. Gago, P. Gazdzicki, T. Morawietz, I. Biswas, R. Schierholz, S. Pylypenko, W. Lehnert, M. Carmo, Investigating the interface of TiOx/PGM coating of porous transport layers used in PEM electrolyzers by surface analysis, in: ECS Meeting Abstracts, 2020, p. 2478, https://doi.org/10.1149/MA2020-02382478MTGABS. MA2020-02 (38).

[11] A. Koni, S. Bliznakov, L.J. Bonville, R. Maric, Reactive spray deposition technology as an alternative method for precious metals deposition on sintered titanium porous transport layers for application in advanced proton exchange membrane water electrolyzers, in: ECS Meeting Abstracts, 2022, p. 1660, https://doi.org/10.1149/MA2022-02441660MTGABS. MA2022-02 (44).

[12] Z. Zhou, R. Yang, Y. Teng, Y. Li, M. Wei, F-Doped TiO2(B)/Reduced graphene for enhanced capacitive lithium-ion storage, J. Colloid Interface Sci. 637 (2023) 533–540, https://doi.org/10.1016/J.JCIS.2023.01.070.

[13] Y. Guo, C.E. Rowland, R.D. Schaller, J. Vela, Near-infrared photoluminescence enhancement in Ge/CdS and Ge/ZnS core/shell nanocrystals: utilizing IV/II-VI semiconductor epitaxy, ACS Nano 8 (8) (2014) 8334–8343, https://doi.org/10.1021/NN502792M/SUPPL_FILE/NN502792M_SI_001.PDF.

[14] Y.F. Nicolau, Solution deposition of thin solid compound films by a successive ionic-layer adsorption and reaction process, Appl. Surf. Sci. 22–23 (1985) 1061–1074, https://doi.org/10.1016/0378-5963(85)90241-7.

[15] M.M. Momeni, Y. Ghayeb, A.A. Mozafari, Optical and photo catalytic characteristics of Ag2S/TiO2 nanocomposite films prepared by electrochemical anodizing and SILAR approach, J. Mater. Sci. Mater. Electron. 27 (11) (2016) 11201–11210, https://doi.org/10.1007/S10854-016-5240-8/METRICS.

[16] J. Torrero, T. Morawietz, D. García Sanchez, D. Galyamin, M. Retuerto, V. Martin-Diaconescu, S. Rojas, J.A. Alonso, A.S. Gago, K.A. Friedrich, High performance and durable anode with 10-Fold reduction of iridium loading for proton exchange membrane water electrolysis, Adv. Energy Mater. 13 (23) (2023) 2204169, https://doi.org/10.1002/AENM.202204169.

[17] N. Kapuria, E. Verma, N. Kar, X. Ye, S.E. Skrabalak, Guiding principles for seeded electrochemical synthesis of multimetallic nanocrystals, Nat. Synth. (2026), https://doi.org/10.1038/s44160-026-01119-z.

[18] K. Lewinski, D. van der Vliet, S.M. Luopa, et al., NSTF advances for PEM electrolysis – the effect of alloying on activity of NSTF electrolyzer catalysts and performance of NSTF based PEM electrolyzers, ECS Trans. 69 (2015) 893–917, https://doi.org/10.1149/06917.0893ecst.

[19] S.H. Park, J. Koo, Y.J. Park, S. Jang, H.J. Ryu, H.S. Han, K.T. Lee, Uniformly scalable and stackable porous transport layer manufactured by tape casting and calendering for efficient water electrolysis, Chem. Eng. J. 481 (2024) 148276, https://doi.org/10.1016/J.CEJ.2023.148276.

[20] K.E. Ayers, C. Capuano, E.B. Anderson, Recent advances in cell cost and efficiency for PEM-based water electrolysis, ECS Trans. 41 (10) (2012) 15–22, https://doi.org/10.1149/1.3684798.

[21] H. Holmquist, P. Fantke, I.T. Cousins, M. Owsianiak, I. Liagkouridis, G.M. Peters, An (Eco)Toxicity life cycle impact assessment framework for per-and polyfluoroalkyl substances, Environ. Sci. Technol. 54 (10) (2020) 6224–6234, https://doi.org/10.1021/ACS.EST.9B07774/ASSET/IMAGES/LARGE/ES9B07774_0002.JPEG.

[22] M.S. Shimizu, R.S. Garcia, G.B. Avery, R.J. Kieber, S.A. Skrabal, R.N. Mead, Distribution of legacy and emerging Per- and polyfluoroalkyl substances in riverine and coastal sediments of Southeastern North Carolina, USA, Environ. Sci. Process. Impacts 24 (11) (2022) 2119–2128, https://doi.org/10.1039/D2EM00246A.

[23] R. Lohmann, I.T. Cousins, J.C. Dewitt, J. Glüge, G. Goldenman, D. Herzke, A. B. Lindstrom, M.F. Miller, C.A. Ng, S. Patton, M. Scheringer, X. Trier, Z. Wang, Are fluoropolymers really of low concern for human and environmental health and separate from other PFAS? Environ. Sci. Technol. 54 (20) (2020) 12820–12828, https://doi.org/10.1021/ACS.EST.0C03244/ASSET/IMAGES/LARGE/ES0C03244_0002.JPEG.

[24] About PFASs - OECD portal on per and poly fluorinated chemicals. https://www.oecd.org/chemicalsafety/portal-perfluorinated-chemicals/aboutpfass/. (Accessed 25 April 2024).

[25] ECHA, *ECHA Publishes Updated PFAS Restriction Proposal*, 20 Aug 2025; ECHA, *ECHA Announces Timeline for PFAS Restriction Evaluation*, 27 Aug 2025. https://echa.europa.eu.

[26] C.S. Gittleman, F.D. Coms, Y.H. Lai, Membrane durability: physical and chemical degradation, Polymer Electrolyte Fuel Cell Degradation (2012) 15–88, https://doi.org/10.1016/B978-0-12-386936-4.10002-8.

[27] US EPA, Interim Guidance on the Destruction and Disposal of PFAS and Materials Containing PFAS, second ed., 2024.

[28] M. Yasutake, D. Kawachino, Z. Noda, J. Matsuda, S.M. Lyth, K. Ito, A. Hayashi, K. Sasaki, Catalyst-integrated gas diffusion electrodes for polymer electrolyte membrane water electrolysis: porous titanium sheets with nanostructured TiO2 surfaces decorated with Ir electrocatalysts, J. Electrochem. Soc. 167 (12) (2020) 124523, https://doi.org/10.1149/1945-7111/ABB37D.

[29] A. Majid, M. Bibi, Wet chemical synthesis methods, Topics in Mining, Metallurgy and Materials Engineering (2018) 43–101, https://doi.org/10.1007/978-3-319-68753-7_3/FIGURES/17.

[30] A.J. Bard, R. Parsons, J. Jordan, Standard Potentials in Aqueous Solution, 2017, pp. 1–834, https://doi.org/10.1201/9780203738764. Standard Potentials in Aqueous Solution.

[31] N.K. Allam, C.A. Grimes, Formation of vertically oriented TiO2 nanotube arrays using a fluoride free HCl aqueous electrolyte, J. Phys. Chem. C 111 (35) (2007) 13028–13032, https://doi.org/10.1021/JP073924I.

[32] F. Ganci, S. Lombardo, C. Sunseri, R. Inguanta, Nanostructured electrodes for hydrogen production in alkaline electrolyzer, Renew. Energy 123 (2018) 117–124, https://doi.org/10.1016/J.RENENE.2018.02.033.

[33] L. Moriau, M. Bele, Ž. Marinko, F. Ruiz-Zepeda, G. Koderman Podboršek, M. Šala, A.K. Šurca, J. Kovač, I. Arčon, P. Jovanovič, N. Hodnik, L. Suhadolnik, Effect of the morphology of the high-surface-area support on the performance of the oxygen-evolution reaction for iridium nanoparticles, ACS Catal. 11 (2) (2021) 670–681, https://doi.org/10.1021/ACSCATAL.0C04741/ASSET/IMAGES/LARGE/CS0C04741_0009.JPEG.

[34] C.B. Mullins, Y.J. Son, K. Kawashima, B.R. Wygant, C.H. Lam, J.N. Burrow, H. Celio, A. Dolocan, J.G. Ekerdt, Anodized nickel foam for oxygen evolution reaction in Fe-Free and unpurified alkaline electrolytes at high current densities, ACS Nano 15 (2) (2021) 3468–3480, https://doi.org/10.1021/ACSNANO.0C10788/SUPPL_FILE/NN0C10788_SI_001.PDF.

[35] A. Touni, A. Papaderakis, D. Karfaridis, G. Vourlias, S. Sotiropoulos, Oxygen evolution reaction at IrO2/Ir(Ni) film electrodes prepared by galvanic replacement and anodization: effect of precursor Ni film thickness, Molecules 24 (11) (2019) 2095, https://doi.org/10.3390/MOLECULES24112095, 2019, Vol. 24, Page 2095.

[36] S.A. Beknalkar, A.M. Teli, N.S. Harale, J.C. Shin, P.S. Patil, Construction of IrO2@Mn3O4 core-shell heterostructured nanocomposites for high performance symmetric supercapacitor device, J. Alloys Compd. 887 (2021) 161328, https://doi.org/10.1016/J.JALLCOM.2021.161328.

[37] S. Shuang, R. Lv, Z. Xie, Z. Zhang, Surface plasmon enhanced photocatalysis of Au/Pt-decorated TiO2 nanopillar arrays, Sci. Rep. 6 (1) (2016) 1–8, https://doi.org/10.1038/srep26670, 2016 6:1.

[38] F. Hegge, F. Lombeck, E. Cruz Ortiz, L. Bohn, M. Von Holst, M. Kroschel, J. Hübner, M. Breitwieser, P. Strasser, S. Vierrath, Efficient and stable low iridium loaded anodes for PEM water electrolysis made possible by nanofiber interlayers, ACS Appl. Energy Mater. 3 (9) (2020) 8276–8284, https://doi.org/10.1021/ACSAEM.0C00735/SUPPL_FILE/AE0C00735_SI_001.PDF.

[39] G. Li, X. Xu, H. Liu, X. Yang, M.C. Lin, Enhanced electrocatalytic performance of IrOx by employing F-Doped TiO2 as support towards acidic oxygen evolution reaction, ChemCatChem 14 (22) (2022) e202201039, https://doi.org/10.1002/CCTC.202201039.

[40] Y. Wei, Z. Wang, J. Wu, B. Liu, Y. Zhang, S. Huang, Effect of oxygen vacancies and F-Doping on TiO2(B) as anode for Mg-Ion batteries, J. Phys. Chem. C 127 (29) (2023) 14086–14097, https://doi.org/10.1021/ACS.JPCC.3C02555/SUPPL_FILE/JP3C02555_SI_001.PDF.

[41] A. Taylor, Practical surface analysis, 2nd edn., Vol I, Auger and X-Ray photoelectron spectroscopy. Edited by D. Briggs & M. P. Seah, John Wiley, New York, 1990, 657 pp., price: £86.50. ISBN 0471 92081 9, J. Chem. Technol. Biotechnol. 53 (2) (1992), https://doi.org/10.1002/JCTB.280530219, 215–215.

[42] V. Pfeifer, T.E. Jones, J.J. Velasco Vélez, C. Massué, M.T. Greiner, R. Arrigo, D. Teschner, F. Girgsdies, M. Scherzer, J. Allan, M. Hashagen, G. Weinberg, S. Piccinin, M. Hävecker, A. Knop-Gericke, R. Schlögl, The electronic structure of iridium oxide electrodes active in water splitting, Phys. Chem. Chem. Phys. 18 (4) (2016) 2292–2296, https://doi.org/10.1039/C5CP06997A.

[43] P. Jovanovič, N. Hodnik, F. Ruiz-Zepeda, I. Arčon, B. Jozinović, M. Zorko, M. Bele, M. Šala, V.S. Šelih, S. Hočevar, M. Gaberšček, Electrochemical dissolution of iridium and iridium oxide particles in acidic media: transmission electron microscopy, electrochemical flow cell coupled to inductively coupled plasma mass spectrometry, and X-Ray absorption spectroscopy study, J. Am. Chem. Soc. 139 (36) (2017) 12837–12846, https://doi.org/10.1021/JACS.7B08071/SUPPL_FILE/JA7B08071_SI_001.PDF.

[44] X. Jiang, C. Kyriakou, C. Wang, S. Costil, C. Deng, T. Liu, T. Jiang, H.A. Liao, Novel multi. -channel porous structure facilitating mass transport towards highly efficient alkaline water electrolysis, J. Energy Chem. 93 (2024) 511–518, https://doi.org/10.1016/j.jechem.2024.02.036.

[45] A.M. Díez, I. Núñez, M. Pazos, M.Á. Sanromán, Y.V. Kolen'ko, Fluoride-doped TiO2 photocatalyst with enhanced activity for stable pollutant degradation, Catalysts 12 (10) (2022) 1190, https://doi.org/10.3390/CATAL12101190/S1.

[46] X. Lin, J.Z.Y. Seow, Z.J. Xu, A brief introduction of electrode fabrication for proton exchange membrane water electrolyzers, J. Phys.: Energy 5 (3) (2023) 034003, https://doi.org/10.1088/2515-7655/ACCCB1.

[47] K. Hirata, K. Akasaka, O. Dopfer, S.I. Ishiuchi, M. Fujii, Transition from vehicle to grotthuss proton transfer in a nanosized flask: cryogenic ion spectroscopy of protonated p-Aminobenzoic acid solvated with D2O, Chem. Sci. 15 (8) (2024) 2725–2730, https://doi.org/10.1039/D3SC05455A.

[48] K.D. Kreuer, Proton conductivity: materials and applications, Chem. Mater. 8 (3) (1996) 610–641, https://doi.org/10.1021/CM950192A/ASSET/IMAGES/MEDIUM/CM950192AN00001.GIF.

[49] T. Reier, D. Teschner, T. Lunkenbein, A. Bergmann, S. Selve, R. Kraehnert, R. Schlögl, P. Strasser, Electrocatalytic oxygen evolution on iridium oxide: uncovering catalyst-substrate interactions and active iridium oxide species,

J. Electrochem. Soc. 161 (9) (2014) F876–F882, https://doi.org/10.1149/2.0411409JES/XML.

[50] S. Geiger, O. Kasian, B.R. Shrestha, A.M. Mingers, K.J.J. Mayrhofer, S. Cherevko, Activity and stability of electrochemically and thermally treated iridium for the oxygen evolution reaction, J. Electrochem. Soc. 163 (11) (2016) F3132–F3138, https://doi.org/10.1149/2.0181611JES/XML.

[51] M.F. Tovini, A.M. Damjanovic, H.A. El-Sayed, J. Speder, C. Eickes, J.-P. Suchsland, A. Ghielmi, H.A. Gasteiger, Degradation mechanism of an IrO2 anode Co-Catalyst for cell voltage reversal mitigation under transient operation conditions of a PEM fuel cell, J. Electrochem. Soc. 168 (6) (2021) 064521, https://doi.org/10.1149/1945-7111/AC0D39.

[52] S. Yuan, C. Zhao, H. Li, S. Shen, X. Yan, J. Zhang, Rational electrode design for low-cost proton exchange membrane water electrolyzers, Cell Rep. Phys. Sci. 5 (3) (2024) 101880, https://doi.org/10.1016/J.XCRP.2024.101880.

[53] C. Liu, B. Mei, Z. Shi, et al., Operando formation of highly efficient electrocatalysts induced by heteroatom leaching, Nat. Commun. 15 (2024) 242, https://doi.org/10.1038/s41467-023-44480-9.